Delft University of Technology

Document Version
Final published version

Licence
CC BY

Citation (APA)
Akrish, G., Reniers, A., Zijlema, M., & Toledo, Y. (2026). Shoreline reflection of free infragravity waves over smooth and rough beds: A SWASH-based numerical study. *Coastal Engineering*, *213*, Article 105159. https://doi.org/10.1016/j.coastaleng.2026.105159

Important note
To cite this publication, please use the final published version (if applicable).
Please check the document version above.

Copyright
In case the licence states “Dutch Copyright Act (Article 25fa)”, this publication was made available Green Open Access via the TU Delft Institutional Repository pursuant to Dutch Copyright Act (Article 25fa, the Taverne amendment). This provision does not affect copyright ownership.
Unless copyright is transferred by contract or statute, it remains with the copyright holder.

Sharing and reuse
Other than for strictly personal use, it is not permitted to download, forward or distribute the text or part of it, without the consent of the author(s) and/or copyright holder(s), unless the work is under an open content license such as Creative Commons.

Takedown policy
Please contact us and provide details if you believe this document breaches copyrights.
We will remove access to the work immediately and investigate your claim.

This work is downloaded from Delft University of Technology.

Coastal Engineering 213 (2027) 105159

Contents lists available at ScienceDirect

Coastal Engineering

journal homepage: www.elsevier.com/locate/coastaleng

Shoreline reflection of free infragravity waves over smooth and rough beds: A SWASH-based numerical study

Gal Akrish [a,b,*], Ad Reniers [b], Marcel Zijlema [b], Yaron Toledo [a]

[a] School of Mechanical Engineering, Tel-Aviv University, Israel
[b] Faculty of Civil Engineering and Geosciences, Delft University of Technology, The Netherlands

ARTICLE INFO

Keywords:
Infragravity waves
Shoreline reflection
Shoreline dissipation
Surfzone hydrodynamics
SWASH
Wave modelling

ABSTRACT

This study presents a numerical investigation of shoreline dissipation and reflection of free infragravity waves. A comprehensive dataset is generated using the SWASH model, covering a wide range of wave and bed conditions. The results show that the contribution of bottom friction to the dissipation of free infragravity waves during shoreline reflection can exceed that of wave breaking, not only for rough beds but also for bed roughness representative of sandy coasts. This challenges the common assumption that bottom friction is of secondary importance and highlights its relevance in controlling infragravity wave reflection.

Motivated by these findings, an empirical model is developed to describe the frequency-dependent reflection of infragravity waves over smooth and rough beds. The model performs well across a broad range of conditions and shows good agreement with laboratory and field observations. It further demonstrates that reflection characteristics strongly depend on incoming wave conditions, cross-shore slope, and bed roughness. Comparison with existing shoreline radiation formulations emphasizes the importance of accounting for these factors in large-scale modelling. The proposed model represents a step forward towards developing an adequate shoreline generation model for free infragravity waves within large-scale modelling frameworks.

1. Introduction

Infragravity (IG) waves are increasingly recognized for their contribution to extreme coastal events, including flooding and erosion (e.g., Dodet et al., 2019). Due to their long wavelengths (ranging from several hundred meters to several kilometers) and low steepness, IG waves can penetrate into very shallow waters with limited dissipation, potentially resulting in highly energetic events (Roeber and Bricker, 2015). Their ability to retain energy across the surfzone allows the IG frequency band to dominate wave runup, overtopping, and overwash, as well as the associated coastal erosion (e.g., Ruggiero et al., 2004; McCall et al., 2010; Baumann et al., 2017). IG waves are also known to excite harbour oscillations (e.g., Bowers, 1977; Okihiro et al., 1993) and are believed to contribute to ice-shelf breakup in polar regions (e.g., Bromirski et al., 2010). With increasing recognition of their impacts, IG waves are now routinely incorporated into early warning systems and coastal safety assessments (e.g., Winter et al., 2020; Lashley et al., 2022).

State-of-the-art modelling frameworks address wave prediction through a coupled large- and small-scale approach (e.g., Turner et al., 2024). Small-scale models propagate wave conditions from offshore boundaries (typically at depths of $O(10)$ m) to the shoreline, resolving nearshore and swash-zone processes (e.g., Roelvink et al., 2009; Zijlema et al., 2011). These models are forced by large-scale models (e.g., SWAN, Booij et al., 1999, WAVEWATCH, Tolman, 1991), which accurately resolve sea-swell energy but typically lack IG wave information. Consequently, IG energy at the offshore boundary is commonly assumed to consist solely of the bound IG (BIG) component, estimated from second-order theory (Hasselmann, 1962). However, observations along open coasts (i.e., coastlines bordering open oceans) have shown that the free IG (FIG) component is often the dominant IG component nearshore and may even govern the IG band under energetic sea-swell conditions (e.g., Okihiro et al., 1992; Elgar et al., 1992; Herbers et al., 1995). In regional seas (e.g., the North Sea, the Mediterranean Sea, the Gulf of Mexico), the FIG-to-BIG energy ratio can be further enhanced by remotely generated FIG waves (e.g., Reniers et al., 2021; Rijnsdorp et al., 2021; Akrish et al., 2025) and may remain significant up to the close vicinity of the shoreline (see recent analyses by Akrish et al., 2025; Reniers et al., 2026b). Therefore, the importance of FIG waves at the offshore boundaries can propagate shoreward and substantially influence nearshore processes, including runup, overtopping, and harbour oscillations, with implications for coastal hazards and maritime operations (e.g., Matsuba et al., 2024).

* Corresponding author at: Faculty of Civil Engineering and Geosciences, Delft University of Technology, The Netherlands.
E-mail address: G.Akrish@tudelft.nl (G. Akrish).

https://doi.org/10.1016/j.coastaleng.2026.105159
Received 17 June 2026; Received in revised form 10 September 2026; Accepted 11 September 2026
Available online 16 September 2026
0378-3839/© 2026 The Authors. Published by Elsevier B.V. This is an open access article under the CC BY license (http://creativecommons.org/licenses/by/4.0/).

In contrast to BIG energy, FIG energy cannot be determined locally but instead results from the superposition of energy contributions generated at different spatial locations and times. As a result, accurate evaluation of FIG waves requires large-scale modelling to account for these distributed spatiotemporal sources. Based on present knowledge, FIG energy originates primarily from nearshore regions due to nonlinear interactions among sea-swell waves (e.g., Webb et al., 1991; Rawat et al., 2014). This introduces a major challenge for large-scale prediction because nearshore FIG wave generation occurs over spatial and temporal scales that are several orders of magnitude smaller than those resolved by large-scale propagation models. Consequently, explicitly resolving the fine-scale generation of FIG waves and their subsequent seaward radiation within large-scale models is not feasible.

To overcome this limitation, Ardhuin et al. (2014) proposed an empirical model to evaluate the seaward radiation of FIG waves along shorelines as a function of the incoming sea-swell field. In this formulation, the radiated FIG energy is assumed to follow a universal spectral distribution (partially justified by linear theory of refractively trapped FIG waves along uniform coasts, see Herbers et al., 1995). The model is based on a correlation parameter α relating the radiated FIG energy to the incident sea-swell conditions (i.e., significant wave height and mean period), and it implicitly accounts for both the shoreward transformation of forced IG waves and the subsequent shoreline reflection of surfzone–released FIG components. Introducing a dependence on coastal properties (e.g., cross-shore slope and bed material), which are known to affect both IG transformation and reflection, requires defining different α values for different coastal types within a given domain (Akrish et al., 2025). This leads to a complex calibration procedure for regions comprising multiple shoreline types. Moreover, the approach does not account for time-varying processes that may influence α, such as incoming sea-swell directionality (see discussion by Rijnsdorp et al., 2021). Finally, it cannot represent the reflection of FIG energy originating from distant coasts.

Recent developments of efficient models for shoreward evolution of forced IG waves (e.g., Vrecica and Toledo, 2019; Reniers and Zijlema, 2022; Akrish et al., 2024; Leijnse et al., 2024; Reniers et al., 2026a) open up the possibility of an alternative approach for describing the seaward radiation of FIG waves along shorelines. This approach is based on separating the processes of shoreward evolution and reflection, under the assumption that in shallow water, sufficiently close to the shoreline, the coupling between sea-swell and forced IG waves weakens (e.g., Ruessink, 1998) and that incoming IG energy can be considered to propagate freely (e.g., Janssen et al., 2003). As a consequence, given the input from forced IG models, this approach is able to combined the locally and remotely generated FIG wave fields and separately compute the reflection of these fields to derived the seaward FIG energy radiation.

To further develop this approach, this study aims to derive an empirical model for shoreline reflection of FIG waves. In the absence of sea-swell and IG wave coupling, the dominant processes governing shoreline reflection are assumed to be dissipation due to wave breaking and bottom friction (e.g., Bertin et al., 2018). The relative importance of these mechanisms remains uncertain and is still subject to ongoing discussion. For sandy beaches, bottom friction is commonly assumed to be negligible (e.g., Van Dongeren et al., 2007; De Bakker et al., 2014), whereas recent observations over rocky coasts suggest that it may play a significant role in determining IG wave reflection (MacMahan et al., 2026). To develop a model applicable across different coastal types, bottom roughness is explicitly included in the formulation. The empirical model is derived from a series of one-dimensional SWASH simulations performed under varying incoming FIG wave conditions, cross-shore slopes, and roughness values. The numerical setup and simulation framework are described in Section 2. Results of FIG wave dissipation and reflection are presented in Section 3, together with the derivation of the empirical shoreline reflection model. Section 4 discusses limitations associated with processes not represented in the SWASH dataset and the derived model (i.e., due to the presence of sea-swell waves and the directional spreading of the incident FIG spectra). This section also examines the relation to the parametrization of Ardhuin et al. (2014) under prescribed incoming FIG conditions. Finally, concluding remarks are presented in Section 5.

2. Wave modelling

2.1. The SWASH model

The estimated FIG energy distribution over sloping shores is obtained numerically using the SWASH model (Zijlema et al., 2011). The considered one-dimensional flume domain is illustrated in Fig. 1. Waves are generated at $x = 0$ m, propagate over a constant depth of $d_0 = 10$ m and shoal over a slope that stretches from $x = 1000$ m up to x_s. The latter spatial point is defined as a function of the slope steepness m as, $x_s = 1000 + (d_0 + 4)/m$, where the addition of 4 m to d_0 is applied to allow enough space for wave runup.

The SWASH model solves the Reynolds-averaged Navier–Stokes (RANS) equations. For an incompressible and inviscid flow within the considered flume settings, these equations are written as

$$\frac{\partial u}{\partial t} + \frac{\partial uu}{\partial x} + \frac{\partial wu}{\partial z} = -\frac{1}{\rho}\frac{\partial p}{\partial x} + \frac{\partial}{\partial x}\left(\nu_h \frac{\partial u}{\partial x}\right) + \frac{\partial}{\partial z}\left(\nu_v \frac{\partial u}{\partial z}\right), \tag{1}$$

$$\frac{\partial w}{\partial t} + \frac{\partial uw}{\partial x} + \frac{\partial ww}{\partial z} = -\frac{1}{\rho}\frac{\partial p}{\partial z} + \frac{\partial}{\partial x}\left(\nu_h \frac{\partial w}{\partial x}\right) + \frac{\partial}{\partial z}\left(\nu_v \frac{\partial w}{\partial z}\right) - g, \tag{2}$$

$$\frac{\partial u}{\partial x} + \frac{\partial w}{\partial z} = 0, \tag{3}$$

$$\frac{\partial \zeta}{\partial t} + \frac{\partial}{\partial x}\int_{-d}^{\zeta} u\, dz = 0, \tag{4}$$

where u and w represent the flow velocities in the horizontal and vertical directions (x, z), and t stands for the time domain. Additionally, ν_h and ν_v are the horizontal and vertical kinematic eddy viscosity terms, p stands for the hydrostatic and non-hydrostatic pressure, g is the gravitational acceleration and ρ is the fluid density. Finally, the flow is bounded by the surface elevation at $z = \zeta(x,t)$ and by the bottom boundary at $z = -d(x)$, while $z = 0$ defines the still water level.

Shoreward propagation of FIG waves involve the formation of bores which may exhibit undulations due to non-hydrostatic effects (e.g., Peregrine, 1966). To model these undular bore transitions, two vertical layers are considered for the vertical resolution. Wave dissipation due to turbulent bore transition is modelled implicitly by enforcing momentum conservation across discontinuities using the nonlinear shallow-water formulation and the default values of $\alpha = 0.6$ and $\beta = 0.3$, controlling the onset and persistence of wave breaking (e.g., Smit et al., 2013). Additionally, bottom friction accounted for by including a stress term, τ_b, in the horizontal momentum balance of the lower layer, formulated through the following quadratic friction law,

$$\tau_b = \frac{n^2 g}{h^{1/3}} \frac{U^2 U_{k2}}{h_{k2}|U_{k2}|}, \tag{5}$$

where n is Manning's roughness coefficient, U is the depth-averaged velocity across the total water depth $h = d + \zeta$ and U_{k2} is the depth-averaged velocity across the height of the lower layer h_{k2}. Finally, to account for vertical mixing due to bottom friction and to increase numerical stability, a constant vertical eddy viscosity value of $\nu_v = 10^{-5}$ m^2/s is introduced, while ν_h assumed to be neglected for the present small-scale wave propagation problem (e.g., Rijnsdorp et al., 2014).

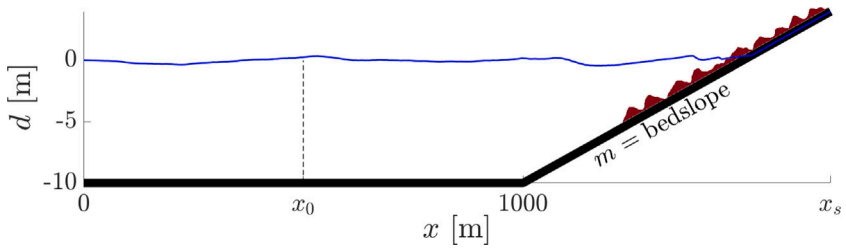


Fig. 1. One-dimensional flume domain used for the SWASH simulations. The dashed vertical line at x_0 = 500 m indicates the location used in Section 3 to determine the reflection quantities for FIG waves. Finally, the shoreline roughness is illustrated over depths smaller than 4 m using the brown fill.

2.2. Energy balance

Starting with (1) and (2), invoking fluid incompressibility (3), applying the kinematic free-surface and bottom boundary conditions and taking the time average (over a short time scale related to the considered wave periods), the energy balance equation can be derived (see detailed derivation by Dingemans, 1997, Section 2.9). Additionally, since the simulations considered here are stationary in time, derivatives of time-averaged quantities are cancelled out. As a consequence, the following energy balance equation is obtained:

$$g\frac{d\bar{F}}{dx} = -D_f - D_b, \tag{6}$$

where $\bar{F}$ denotes the depth-integrated and time-averaged energy density flux (normalized by g) and D_f and D_b are the dissipation terms arising due to bottom friction and wave breaking, respectively. Based on the bottom friction formulation considered here, D_f can be calculated explicitly as

$$D_f = -\left\langle \int_{-d}^{-d+h_{k2}} u\tau_b \, dz \right\rangle, \tag{7}$$

where $\langle ... \rangle$ indicates time average. Substituting (5) for τ_b leads to the following expression for D_f:

$$D_f = -\left\langle \frac{n^2 g}{h^{1/3}} U^2 |U_{k2}| \right\rangle, \tag{8}$$

To gain insights into the relative contribution of wave breaking and bottom friction within the process of shoreline reflection of FIG waves, (6) is integrated over the cross-shore domain, yielding

$$\bar{F}(x_s) - \bar{F}(x) = -\frac{1}{g}\int_x^{x_s} \left(D_f + D_b\right) dx'. \tag{9}$$

where $\bar{F}(x_s) = 0$ as x_s is located beyond the swash zone where wave motion is absent (see the location x_s in Fig. 1). Ultimately, by distinguishing between incoming and outgoing energy fluxes, $\bar{F}^{\pm}$, and dividing by $\bar{F}^{+}$, the total dissipation due to wave breaking throughout the process of shoreline refection, and the separated contribution of the two dissipation mechanisms as evaluated at x, can be estimated using

$$R^2 = 1 - \frac{\int_x^{x_s} D_f \, dx'}{g\bar{F}^{+}} - \frac{\int_x^{x_s} D_b \, dx'}{g\bar{F}^{+}}, \tag{10}$$

where the reflection coefficient R^2 is defined as

$$R^2 = \frac{\bar{F}^{-}}{\bar{F}^{+}} \tag{11}$$

and the cross-shore integration of D_f is evaluated based on (8). This derivation is completed by introducing the method of separating between incoming and outgoing waves. To this end, the linear shallow water formulation of Guza et al. (1984) is employed, for which,

$$\zeta^{\pm} = \frac{1}{2}\left(\zeta \pm \frac{Q}{\sqrt{gh}}\right) \tag{12}$$

and accordingly,

$$\bar{F}^{\pm} = \sqrt{gh}\ \bar{E}^{\pm} \tag{13}$$

where $Q = hU$ is the discharge and $\zeta^{\pm}$ and $\bar{E}^{\pm}$ define the surface elevation due to incoming and outgoing waves and the corresponding variances (i.e., $\bar{E}^{\pm} \equiv \left\langle \zeta^{\pm 2} \right\rangle$). In the frequency domain, the incoming and outgoing variance spectra are denoted by $E^{\pm}$ (with dimensions [m^2/Hz]). Similarly, $F^{\pm}$ denotes the incoming and outgoing variance flux spectra (with dimensions [m^3]). Note the use of the total water depth in (12) and (13), a modification which reduces to the original formulation of Guza et al. (1984) for $\zeta/h \ll 1$, but produces more reliable results close to the shoreline where $\zeta/h \approx 1$ (also see related formulations by Dekkers, 2018, Section 4).

2.3. Boundary conditions and numerical settings

In order to develop an empirical model for shoreline reflection of FIG waves and to gain insights into the importance of breaking and bottom friction dissipation across different coastal settings, a wide range of wave and bed conditions is considered. At the incoming boundary, only FIG energy is imposed. Sea-swell waves are excluded from the incident wave field, but used to define the frequency distribution of the incoming FIG energy through second-order theory (Hasselmann, 1962). The principle assumption made here is that the shoreward propagating FIG spectrum can be approximated based on the bound IG (BIG) spectrum, calculated using second-order theory and estimated at a point further seaward than the sea-swell breakpoint. The water depth at this offshore point is assumed to follow the value $h = H_{ss}/0.3$, where H_{ss} is the significant wave height of the incoming sea-swell field. This water depth is expected to exceed that of the sea-swell breakpoint, which is usually assumed to be $h \approx H_{ss}/0.45$ (e.g., Holthuijsen, 2010), and for which second-order theory is usually no longer valid and overestimates the incident IG energy. Using these assumptions, the considered incoming FIG conditions are directly obtained given the incoming sea-swell conditions. The latter are assumed to follow a JONSWAP structure in frequency domain and a powered cosine structure (i.e., $\cos^p\theta$) in the directional domain. Thus, the sea-swell conditions are defined based on the values of H_{ss}, the peak period T_p, the peak enhancement factor γ and the directional spreading σ_θ (or the cosine power p). It is important to emphasize here the use of the two-dimensional sea-swell spectra to define the incoming one-dimensional FIG wave fields (contributions of IG response in different directions are summed for each IG frequency). This is performed to construct more diverse and realistic incoming FIG conditions.

The considered range for the sea-swell wave height is $H_{ss} \in [1, 4]$ m. This range is selected to produce significant IG responses while ensuring that strong nonlinearity develops only at depths shallower than approximately 4 m. As a result, shoreline reflection and the associated wave breaking and bottom friction dissipation are largely confined to the immediate vicinity of the shoreline. The range of H_{ss} determines the range for the mean wave period $T_{m-1,0}$ through the offshore wave steepness S_0, defined based on linear deep water wave theory as,

$$S_0 = \frac{2\pi H_0}{gT_0^2} \tag{14}$$

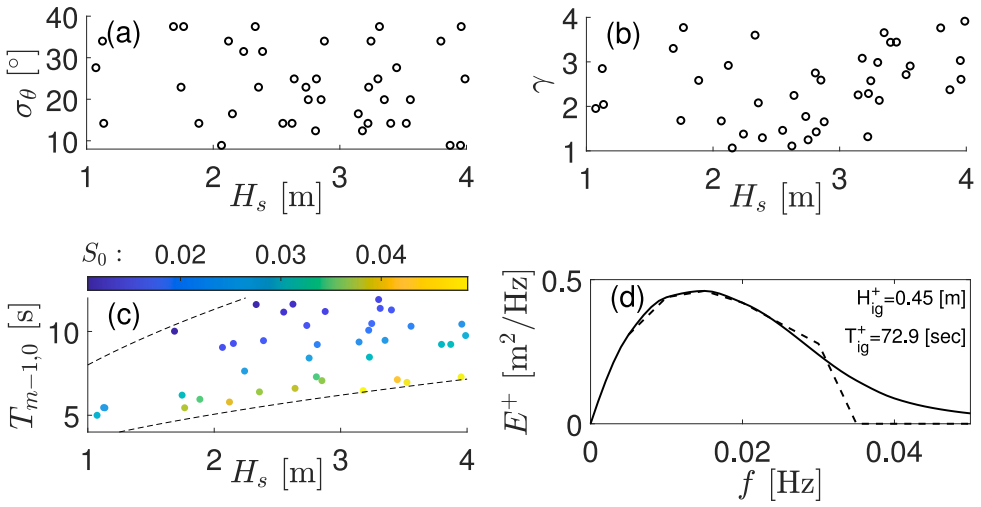


Fig. 2. Incoming sea-swell and IG wave conditions. Panels (a–c) shows the random selection of sea-swell parameters within defined ranges and limited steepness values (S_0), indicated by the dashed curves in panel (c). Panel (d) presents an example of the resulting IG spectra, where the dashed curve illustrates the (directionally integrated) BIG wave response and the solid curve describes the assumed incoming FIG spectrum.

where $H_0 = H_{ss}$ and $T_0 = T_{m-1,0}$. The offshore wave steepness usually falls below 0.05 (e.g., Holthuijsen, 2010, Figure 6.23). Limiting the analysis to wave steepness values within $S_0 \in [0.01, 0.05]$ leads to the period range of about $T_{m-1,0} \in [4, 12]$ s where the corresponding T_p is then estimated as $T_p = 1.125\ T_{m-1,0}$ (e.g., Ahn, 2021). Additionally, the peak enhancement factor γ and the directional spreading σ_θ are selected randomly from $\gamma \in [1, 4]$ and $\sigma_\theta \in [8.9, 37.5]°$. The latter correspond to the cosine power range of $p \in [1, 40]$ (i.e., $p = 1$ corresponds to $\sigma_\theta = 37.5°$, while $p = 40$ corresponds to $\sigma_\theta = 8.9°$). In total, 40 different sea-swell conditions are considered. These are described in Fig. 2 together with an example of a resulted incoming FIG spectrum. Finally note that the forced BIG spectra are computed for the frequency range of $f \in [0.005, 0.03]$ Hz, whereas the incoming FIG spectra are defined by interpolating and extrapolating the BIG response over the frequency range of $f \in [0.001, 0.05]$ Hz using a frequency step of $\Delta f = 0.001$ Hz, and assuming that $E^+(f = 0) = 0$ and that $E^+(f) \propto f^{-4}$ for $f > 0.03$ Hz (following the frequency distribution structure found to characterize wave runup, Huntley et al., 1977).

In addition to wave conditions, variations in seabed properties are considered. Bed conditions are parameterized using the cross-shore slope steepness m and Manning's roughness coefficient n. The bed slope is varied over the range $m \in [0.005, 0.1]$, representing coastal profiles from very gently sloping beaches to steep nearshore and coastal faces. Manning's roughness coefficient is prescribed within the range $n \in [0, 0.06]$ sm$^{-1/3}$, encompassing hydraulically smooth (e.g., fine sand or silt, with typical values of $n \approx 0.01$ sm$^{-1/3}$) to highly rough coastal surfaces (e.g., cobble- or boulder-dominated coasts or sparsely vegetated areas, with typical values of $n \approx 0.03 - 0.06$ sm$^{-1/3}$).

The adopted roughness ranges follow established guidance for coastal and hydraulic applications, including classical and widely used engineering references (e.g., Chow, 1959; Arcement and Schneider, 1989) and more recent large- and regional-scale coastal modelling studies (e.g., Bunya et al., 2010; Mackie et al., 2021). In this study, the impact of bottom roughness is discussed using four representative n values corresponding to smooth, sandy, rocky, and vegetated coast types. These coastal categories and their associated roughness values are summarized in Table 1 and are referred to interchangeably throughout the text.

Finally, all the numerical simulations considered here are performed using spatial step of $\Delta x = 0.5$ m, time step of $\Delta t = 0.025$ s and simulation time of 60 min, from which the first 1600 s are defined as the spinup time and are disregarded from time-averaged quantities.

Table 1
Representative Manning's roughness values for commonly encountered coasts.

Coast type	Representative n [s m$^{-1/3}$]
Smooth	$n = 0$
Sandy	$n = 0.02$
Rocky	$n = 0.04$
Vegetated	$n = 0.06$

3. Results

3.1. Spatial distribution of FIG wave dissipation and reflection

The FIG wave conditions illustrated in Fig. 2(d) represent the most extreme conditions (in terms of H^+_{ig}) included in the SWASH dataset. These incoming conditions, combined with a bottom slope of $m = 1/50$, are used here to examine nearshore FIG wave evolution and the contributions due to wave breaking and bottom friction for the four representative coast types of Table 1. The surface elevation obtained for each coast type is described over very shallow water depths and in the swash zone in Fig. 3. Using (12), the upper panel in Fig. 3 describes the incoming wave field at depths where wave crests pitch forward and, for steeper waves, develop into undular bores, resulting in rapid oscillations at the wave front (Peregrine, 1966). The lower panel shows the total surface elevation within the shallower swash zone, where these undular bores have already undergone substantial attenuation. At $d = 1$ m, differences between the results are small. However, over shallower depths and within the swash zone, the influence of the Manning coefficient n leads to increasingly large discrepancies. Over shallow depths and for higher n values (see Fig. 3(a)) the bores appear milder and their associated undulations are characterized by smaller amplitudes, indicating the impact of bottom friction on the energy transfer to higher harmonics and the associated high-frequency wave dissipation due to breaking. Over the swash zone (see Fig. 3(b)), the accumulated effect of bottom friction appears significant, leading to lower amplitudes running-up shoreward for larger n values .

The impact of the Manning coefficient n on the bore evolution is also reflected in the results of H^+_{ig} (see Fig. 4(b)). As shown in Fig. 3, higher n values lead to smaller amplitudes of developed undular bores, resulting in lower H^+_{ig} values prior to wave breaking (compare H^+_{ig} for $n = 0$ and $n > 0$ at $d \approx 0.8$ m). The influence of bottom friction on the bore evolution in the surfzone considerably reduces FIG wave

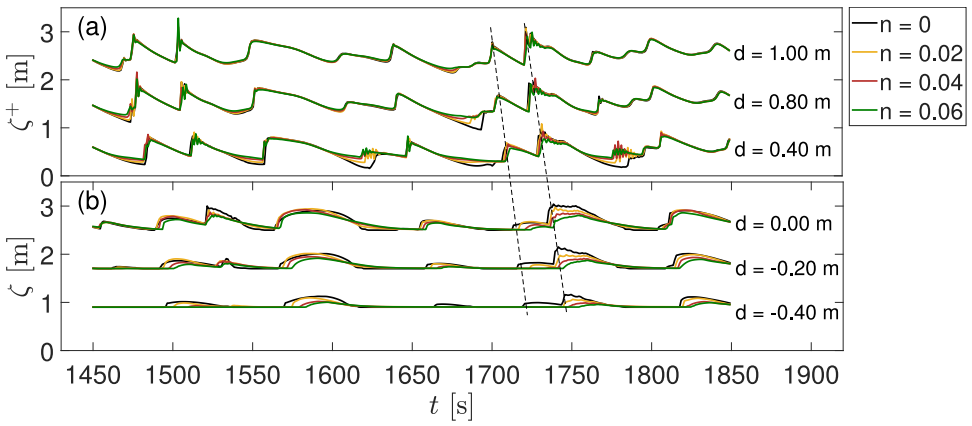


Fig. 3. Free-surface elevation of (a) incoming and (b) total wave fields propagating over a 1:50 slope for the wave conditions described in Fig. 2(d).

energy reflection, as demonstrated in Fig. 4(a). Even for sandy coasts, represented by $n = 0.02$, bottom friction reduces the reflected energy by approximately 50% compared to that reflected from a smooth coast ($n = 0$). Similar comparisons for n values characterizing rocky or vegetated coasts show reductions of about 75%.

Expressions (5) and (10) allow the separation between the contributions of wave breaking and bottom friction throughout the reflection process. This separation is illustrated for the present case in Fig. 4(c), revealing the following insights. Particularly, the importance of wave dissipation due to bottom friction is clearly demonstrated. It is shown that bottom friction can be the leading dissipation mechanism throughout the FIG shoreline reflection for coasts characterized by relatively high n values (e.g., rocky coasts). Surprisingly, bottom friction dissipation also presents significant contribution for n values characterizing sandy coasts. For example, Fig. 4(c) shows that the normalized integrated bottom friction contribution for $n = 0.02$ at $d = 4$ m provides a value of 0.28, while the corresponding contribution of wave breaking is 0.54. This finding contradicts the common assumption that bottom friction plays a secondary role for sandy beaches (e.g., De Bakker et al., 2014). Additionally, the results show the reduction in the contribution of wave breaking for higher n values, which again indicates the effect of bottom friction on the bore evolution and the associated higher harmonic generation and dissipation, and emphasizing the coupling exists between these two dissipation mechanisms throughout the reflection process. This coupling is further illustrated over shallower depths where both mechanisms are of similar importance and the role of the leading mechanism changes (see Fig. 4(c) for $d < 1$ m). An example for that is provided by the results of $n = 0.02$, for which breaking is the primary dissipation mechanism of the entire reflection process but bottom friction takes over the leading role for very shallow water depth (i.e. $d < 0.4$ m). An opposite result is obtained for $n = 0.06$, where the primary dissipation mechanism of the entire reflection process is the bottom friction (as shown by Fig. 4(c) for $d > 2$ m), while wave breaking takes over the leading role close to the shoreline.

Additional insights into the effect of bottom friction on the incoming wave evolution and the resulting reflection is obtained by examining the evolution of the variance density of the free-surface elevation ζ in the frequency domain. This evolution is illustrated in Fig. 5. Comparing the results for different n values, the incoming variance appears equivalent for $d > 1$ m, whereas noticeable discrepancies arise for $d < 1$ m. This observation is consistent with the results shown in Figs. 3 and 4. Fig. 4(c) indicates that substantial dissipation due to bottom friction accumulates already at depths of $d = 1$ m and $d = 0.8$ m. This is also reflected in Fig. 5, when comparing the results for $n = 0.06$ with those for $n = 0.02$ and $n = 0$. Dissipation over the frequency band around the peak frequency f_p can reduce energy transfer to higher harmonics (see vertical dashed lines in Fig. 5, which indicate the frequency bands associated with f_p and its higher harmonics $2f_p$ and $3f_p$). This effect can partially explain the lower variance levels observed at higher frequencies for larger n values (see the results of $d = 1$ m $d = 0.8$ m). Additionally, note that based on the present results, energy transfer to frequencies beyond the IG band (i.e., $f > 0.05$ Hz) seems negligible. Finally, the results clearly demonstrate a decrease in outgoing variance with increasing n. Moreover, the outgoing and incoming variance spectra indicate that dissipation is more pronounced at higher frequencies, while the ratio of outgoing to incoming variance approaches unity at very low frequencies. This trend is quantified in Fig. 5 through the frequency-dependent reflection, $R_f^2 = E^-/E^+$.

3.2. Bulk dissipation and reflection

The complete range of wave and bathymetry conditions defined in Section 2 allow to gain insights into the manner these conditions controlling shoreline dissipation and reflection quantities. This is examined here in terms of the bulk quantities of wave dissipation and reflection evaluated at x_0, a point located away from the nonlinearity region characterizing the shoreline environment (see Fig. 1). Therefore, these bulk results represent the outcome of the complete shoreline reflection process, encompassing nonlinear wave evolution and bore formation and the total wave dissipation across the surf and swash zones.

Fig. 6 presents the contribution of the different dissipation mechanisms as a function of the cross-shore slope m and for different roughness and wave conditions. Since milder slopes essentially correspond to wider spatial region of shallow waters, stronger dissipation is expected to accumulated as m decrease. This expectation is indeed presented in Fig. 6. Additionally, as expected, higher H_{ig}^+ values lead to higher contribution of wave breaking (compare upper panels of Fig. 6). As revealed by the lower panels of Fig. 6, the dependence of the dissipation due to bottom friction on H_{ig}^+ is less straightforward. Particularly, the panels show that in contrast to steep slopes (i.e., $m \geq 0.04$), for mild slopes, the contribution of bottom friction decreases for higher H_{ig}^+ values. This counter-intuitive observation can be explained through the coupling between the two dissipation mechanisms. In general, cases characterized by very mild slopes allow for a significant accumulation of dissipation due to wave breaking at depths where the effect of bottom friction may still be negligible. The accumulation of breaking dissipation would be intensified for higher H_{ig}^+, so that a situation may occur where increased H_{ig}^+ leads to a lower bed velocity where friction begins to play an important role and thus to lower integrated values of friction dissipation.

The coupling between the two dissipation mechanisms also leads to a decrease in the dissipation values as m decreases for very mild slopes, as is shown by the upper panels of Fig. 6 for $n = 0.04$ and $n = 0.06$ and by the lower panels for $n = 0.02$. Note that for rough surfaces, a reversed coupling effect occurs, resulting in decreased integrated breaking dissipation due to increased accumulation of dissipation due

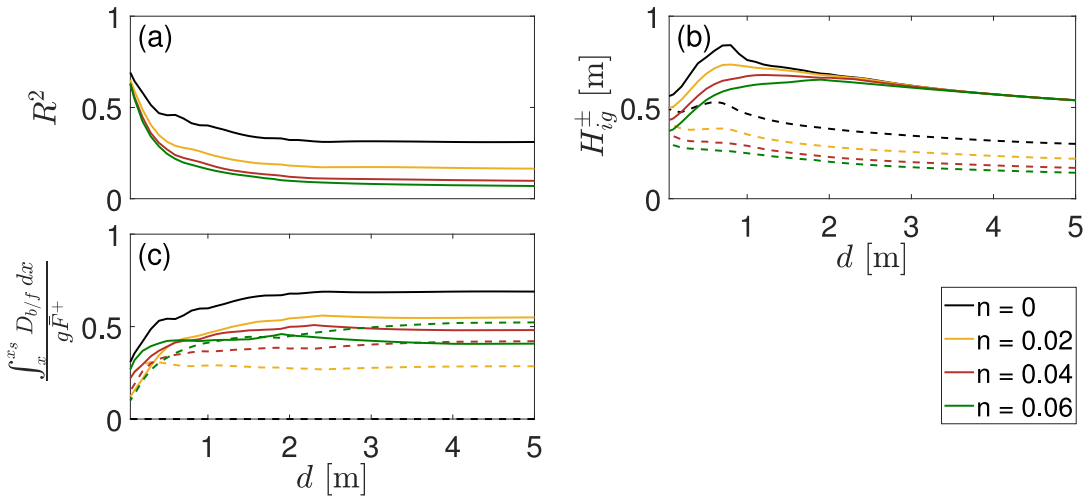


Fig. 4. Spatial distribution of (a) FIG wave reflection, (b) incoming (solid lines) and outgoing (dashed lines) significant wave heights and (c) normalized integrated contributions of wave breaking (solid lines) and bottom friction (dashed lines) dissipation mechanisms. Results are obtained for $m = 1/50$ and the wave conditions presented in Fig. 2(d).

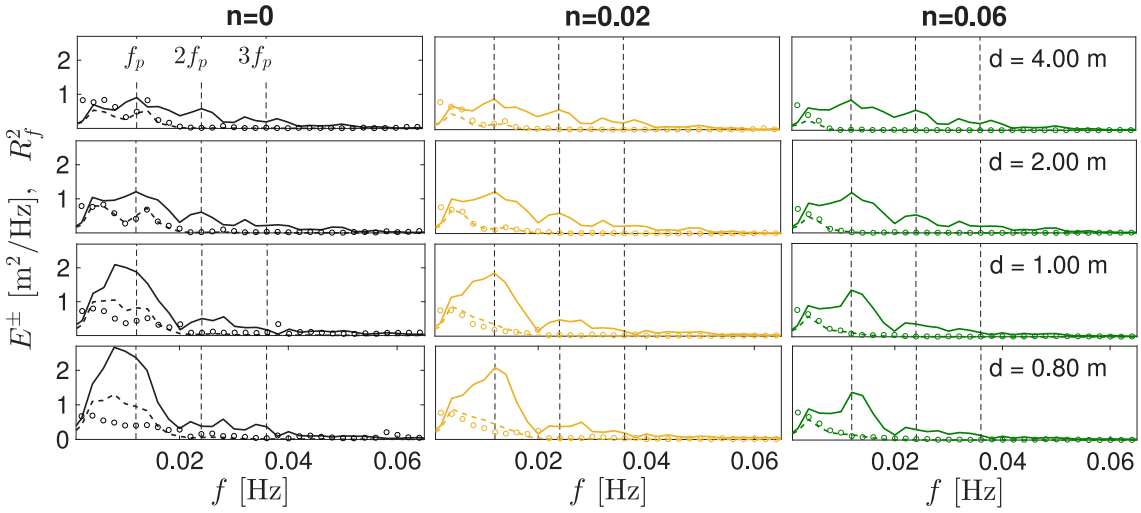


Fig. 5. Frequency-dependent reflection R_f^2 (circles) and incoming (solid lines) and outgoing (dashed lines) variance densities $E^{\pm}$. The vertical dashed lines indicate the frequency regions of the peak frequency f_p and its higher harmonics $2f_p$ and $3f_p$.

to bottom friction. This coupling generates a clear classification for very mildly sloping coasts, for which FIG wave dissipation over coasts characterized by relatively smooth surfaces is expected to be dominated by wave breaking, whereas over rough surface coasts, dissipation is expected to be controlled by the bottom friction. Over steeper slopes the classification in terms of the roughness parameter is less clear. However, the fact that the breaking dissipation decreases much more rapidly compared to the decrease of the friction dissipation as m increases, may indicate that the latter tends to become the primary dissipation mechanism for steep coasts.

The ratio of the two dissipation mechanisms is shown as a function of m, for different values of n and H_{ig}^{+} in a direct manner in Fig. 7. The fact that most of the presented dots lie above the horizontal dashed line (representing a ratio of one) indicates the relative importance of bottom friction dissipation. As shown in Fig. 7, this relative importance depends on m, n and H_{ig}^{+}. The discussed classification for very mild slopes is clearly observed. Additionally, for steeper slopes, the dissipation ratio obtains a maximum at an m value that depends on n and H_{ig}^{+} and can exceed 2 for all three values, $n = 0.02$, 0.04 and 0.06 sm$^{-1/3}$. This finding further emphasizes the potential importance of bottom friction for sandy coasts. In particular, the results indicate that for $m \geq 0.05$ (a steepness range representative of, e.g., the sandy coastline at the Field Research Facility in Duck, North Carolina, see Fig. 4 in Elgar et al., 1994), the contribution of bottom friction to FIG dissipation exceeds that of wave breaking, even under energetic wave conditions. This clearly deviates from the common assumption that bottom friction plays a secondary role on sandy beaches (see Bertin et al., 2018, Section 3.2 and references therein). Instead, the results suggest that, depending on the beach slope and incoming wave conditions, bottom friction can substantially contribute to the dissipation of FIG waves over sandy coasts.

Based on the complete set of SWASH runs and following the importance of the two dissipation mechanisms, it is attempted here to derive a generalized parametrization for the bulk reflection R^2 (see its definition in (11)), taking into account the cross-shore slope, the incoming wave conditions and the bed roughness. Parametrizations for R^2 were previously proposed for the sea-swell frequency band based on the Miche number M or the Iribarren number ξ (see Miche, 1951; Battjes, 1974). These can be expressed as

$$R^2 = \min(M, 1), \tag{15}$$

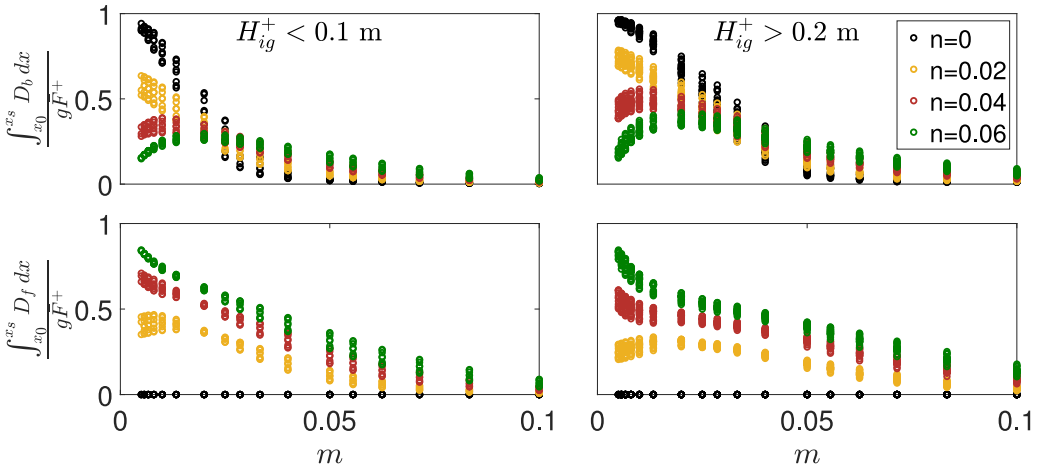


Fig. 6. Normalized integrated contributions of wave breaking (upper panels) and bottom friction (lower panels) dissipation mechanisms as a function of the cross-shore slope, for relatively mild (left panels) and high (right panels) incoming FIG conditions. The integration is evaluated at x_0, see Fig. 1.

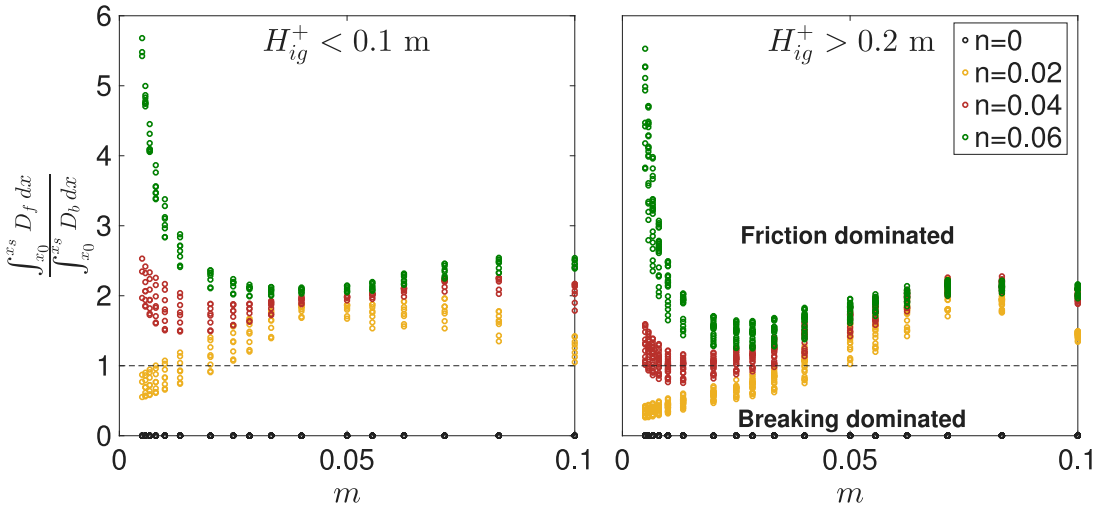


Fig. 7. The ratio between the integrated contributions of bottom friction and wave breaking as a function of the cross-shore slope for relatively mild (left panel) and high (right panel) incoming FIG conditions. The horizontal dashed lines indicate equal contributions.

and

$$R^2 = \min\left(0.01\left(\sqrt{2\pi}\beta_H\right)^4, 1\right), \tag{16}$$

where, recalling the definition of S_0 in (14), M is defined as,

$$M = \frac{16m^5}{(2\pi)^3 S_0^2}, \tag{17}$$

and $\beta_H = \xi/\sqrt{2\pi}$ is a scaled Iribarren number (commonly used in the literature to characterize the reflection of IG waves, see Van Dongeren et al., 2007), defined as

$$\beta_H = \frac{m}{\sqrt{2\pi S_0}} \tag{18}$$

Note that these numbers essentially express a certain ratio between the cross-shore slope steepness, m and the incoming wave steepness S_0, using different emphasis on each of these steepnesses. The relation between β_H and M can be expressed as

$$M = \frac{16}{2\pi} m \beta_H^4 \tag{19}$$

This relation suggests that compared to β_H, M emphasizes more the role of m in predicting the degree of wave reflection. Fig. 8 presents the suitability of the parametrizations (15) and (16) to describe the reflection of FIG waves based on the numerical dataset collected here. In addition to these earlier parametrizations, more recent formulations suggested by Eq. 13 of Ardhuin and Roland (2012) and by Eq. 5 of Zanuttigh and Van der Meer (2006) are plotted as well. Note that the M-based parametrizations are computed based on $T_{m0,1}$ (as also used by Elgar et al., 1994; Ardhuin and Roland, 2012), while the β_H-based parametrizations are calculated using $T_{m-1,0}$ (as suggested by Zanuttigh and Van der Meer, 2006). Additionally, H_{ig}^{+} is used to represent the incoming wave height for all the parametrizations considered here.

Fig. 8 emphasizes once again the significant role of bed friction within the reflection process, showing significant decrease of R^2 for higher n values. The results also show that for $n = 0$, β_H-based parametrizations (derived based on data of rather steep slopes, see Figure 2 in Battjes, 1974) overestimate the computed R^2 of FIG waves, while M-based parametrizations (found suitable for sea-swell reflection from sandy slopes of $m \in [0.05, 0.1]$, see Figure 5 in Elgar et al., 1994) mostly underestimate the modelled reflection of FIG energy. Additionally, Fig. 8(b) shows the transition from mild- to steep-sloping regime (indicated by the four blue circles), defined here following the criterion proposed by De Bakker et al. (2016) for irregular wave reflection. In contrast to the transition identified by Van Dongeren et al. (2007) at $\beta_H = 1.25$, Fig. 8(b) suggests that this transition occurs at higher β_H values for relatively smooth beds (as also observed

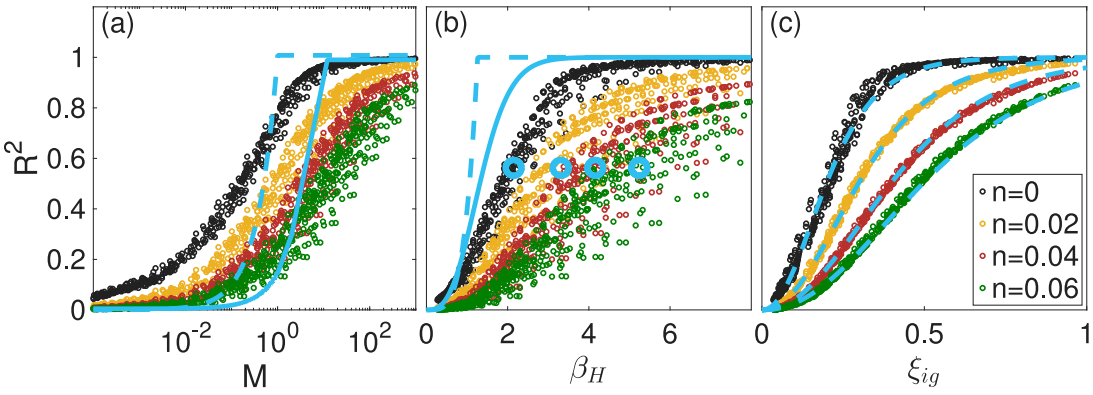


Fig. 8. Bulk energy reflection as a function of (a) Miche number, (b) Iribarren number and (c) the parameter proposed in (20) (i.e., with $r = 5$). The blue dashed lines represent the parametrizations proposed by (a) Miche (1951), (b) Battjes (1974) and (c) Eq. (21), while the blue solid lines show the parametrizations proposed by (a) Ardhuin and Roland (2012) and (b) Zanuttigh and Van der Meer (2006). The four blue circles in the centre of panel (b), each corresponding to one of the four n values, indicate the transition from the mild- to steep-sloping regime and represent the average β_H value for which $R = 0.75 \pm 0.05$ (i.e., $R^2 \approx 0.56$).

by De Bakker et al., 2014, 2016) and shifts to progressively higher values as bed roughness increases. Finally, note that the spread of the reflection results appear to be more significant based on β_H, indicating an improved characterization of the FIG reflection by emphasizing the role of m, as suggested in the definition of M.

Following these observations it is attempted here to find a generalized reflection parametrization that can be adequately applied to characterize wave reflection for the FIG band over smooth and rough beds. This is performed by considering first the following more general ratio definition between m and S_0 represented through the parameter ξ_{ig}:

$$\xi_{ig} = \frac{m}{S_0^{1/r}} \tag{20}$$

for which $r = 2.5$ recovers the ratio embedded in M and $r = 2$ recovers the ratio defined by β_H. Furthermore, based on the observed tangent-hyperbolic trend of the results, which also found to characterize the datasets used by Zanuttigh and Van der Meer (2006), the following formula is proposed for the bulk reflection of FIG waves:

$$R^2 = \tanh^p(\alpha \xi_{ig}) \tag{21}$$

By searching the parameters that minimize the mean-absolute-error with respect to the SWASH dataset, it is found that FIG wave reflection is most adequately described using $r = 5$ and $p = 2.15$, where ξ_{ig} is defined with $T_{m-1,0}$. Repeating the optimization for different values of n yields the functional form of α, expressed as

$$\alpha = c \frac{n_0}{n + n_0} \tag{22}$$

where c and n_0 are found to be $c = 4.63$ and $n_0 = 0.04$ sm$^{-1/3}$. The obtained generalized parametrization is compared with the SWASH results for different n values in Fig. 8, showing close agreement.

3.3. Frequency-dependent reflection

Using the bulk reflection model (21) and (22) as a starting point, an attempt is made here to characterize the steepness of the incoming wave based on the frequency space variables F^+ and f instead of the bulk parameters H_{ig}^+ and $T_{m-1,0}$, thereby enabling a description of the frequency-dependent reflection R_f^2. Accordingly, the following formulation is proposed:

$$R_f^2 = \tanh^p\left[\frac{n_0 m}{n_0 + n}\left(\frac{g^{1.5}}{c\sqrt{F^+} f^3}\right)^{1/r}\right] \tag{23}$$

Table 2
Optimal parameter values of the empirical model (23) for predicting frequency-dependent FIG reflection.

n_0 [s m$^{-1/3}$]	p	c	r
0.04	5	1.5	3.75

Note that the use of F^+ leads to a formulation of R_f^2 that remains invariant under linear shoaling. Additionally, the use of frequency space variables, avoids sensitivity to different definitions of the IG frequency band or to different definitions of bulk parameters (e.g., $T_{m-1,0}$ or $T_{m0,1}$). Finally, the desired non-dimensionality of the right-hand-side of (23) can readily be verified.

The optimal parameter values of the proposed reflection model are found based on a randomly selected subset of one hundred SWASH simulations satisfying $H_{ig}^+ > 0.2$ m. These values minimize the sum of the absolute errors, each of which is defined as:

$$\mathrm{err}_j = \left| \int_{0.004}^{0.05} \frac{E_p^-}{E^+} df - \int_{0.004}^{0.05} \frac{E_m^-}{E^+} df \right|_j \tag{24}$$

where E_p^- and E_m^- are the outgoing variance spectra predicted using (23) and SWASH, respectively. The obtained optimal parameter values are summarized in Table 2, where it should be noted that also here the optimal result is obtained for $n_0 = 0.04$ sm$^{-1/3}$. Moreover, the formulation approaches unity at very low frequencies. Over higher frequencies, the formulation yields the following asymptotic result:

$$E^- \propto F^{+1/3} f^{-4} \tag{25}$$

Assuming that $F^{+1/3}$ is relatively flat, this result suggests that E^- closely follows an f^{-4} spectral decay at higher frequencies, similar to the high-frequency power law observed in vertical runup spectra on natural beaches (Huntley et al., 1977).

Although the empirical model (23) is insensitive to linear shoaling, it may still produce different results at different depths within the IG shoaling zone due to bottom friction. Since the model is calibrated for bottom friction applied at $d \leq 4$ m, a correction factor may be required if the reflection is considered at deeper or shallower depths than 4 m. In most practical applications, however, this correction is expected to be small since frictional dissipation becomes significant only in very shallow water near the shoreline. Exceptions may arise for unusually large propagation distances, over which frictional dissipation can accumulate, or for extremely rough beds. For completeness, a correction factor is proposed in Appendix A.

Model verification is performed through comparison with SWASH using a set of randomly selected cases that were not considered in the

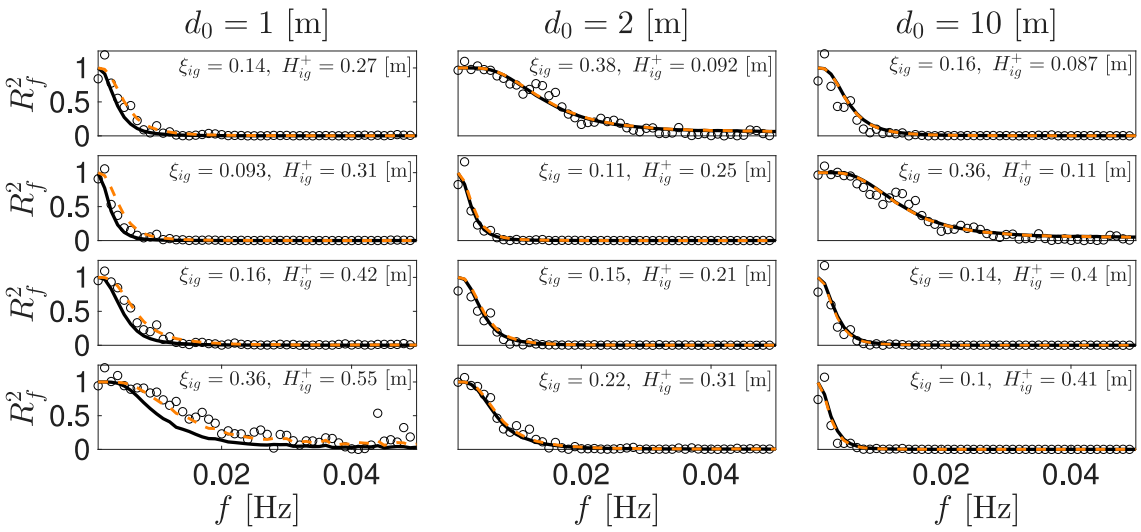


Fig. 9. Verification of the empirical model (23) against SWASH using cases not included in the optimization phase. Predictions without bottom friction correction (solid lines), with bottom friction correction (dashed lines; see Appendix A), and SWASH results (circles) are compared for $n = 0.06$ sm$^{-1/3}$ and randomly selected values of ξ_{ig}.

model development. These cases are designed to test the robustness of (23) by considering the reflection at depths both shallower and deeper than $d = 4$ m for waves propagating over a rough bed (applying $n = 0.06$ sm$^{-1/3}$). The verification is presented in Fig. 9, where each column of panels describes the reflection at a certain depth d_0 for different combinations of wave and slope conditions (represented by ξ_{ig}). The results of (23) with and without the correction for bottom friction (see the formulation for this correction in Appendix A) suggest that in most cases, especially for $d_0 > 4$ m, the correction leads to a negligible contribution. However, for $d_0 = 1$ m, the added value of this correction becomes more significant (see comparisons of the left column of panels in Fig. 9). These results suggest that this correction becomes important only under extreme cases of very shallow depth (where d_0 already falls within or very close to the IG surfzone) and very rough beds (not shown here are repeated results for $d_0 = 1$ m using $n = 0.03$ sm$^{-1/3}$ for which the correction returns to be negligible). Finally refer to the close agreement between (23) and SWASH under various conditions, including moderate (i.e., $H_{ig}^+ \approx 0.1$ m) and rather high (i.e., $H_{ig}^+ \approx 0.4$ m) incoming FIG wave heights and for different values of ξ_{ig}.

The empirical model (23) essentially estimates E^- as a function of E^+, m and n. To examine the dependency of the reflected FIG variance spectrum on m and n under significant wave conditions, E^- is evaluated for the incoming conditions described in Fig. 2(d) and for different values of m and n. Fig. 10 compares the outcome of this evaluation using SWASH, the empirical model (23) and the parametrization proposed by Battjes (1974) (i.e, (16)). The latter is calculated considering β_H to be a frequency-dependent parameter (see Eqs 17-18 in Reniers et al., 2026a). This is performed by defining the wave steepness S_0 through $T_0 = 1/f$ and $H_0 = H_{ig}^+$, which results in

$$\beta_H = \frac{m}{2\pi f}\sqrt{\frac{g}{H_{ig}^+}} \tag{26}$$

Fig. 10 emphasizes the importance of both parameters m and n for the determination of the reflected spectrum. The impact of m is clearly demonstrated by comparing the columns of the panels of Fig. 10, where reflected energy levels decrease significantly as m decreases due to wave breaking and bottom friction dissipation (as also suggested in Fig. 6). Energy also decreases as n increases. This is already evident when comparing the $n = 0$ case with results representative of sandy beaches (i.e., $n = 0.02$), emphasizing once again the importance of bottom friction in the reflection process for these types of coasts. Finally, the results of $n = 0$ demonstrate the overestimation of the parametrization by Battjes (1974). For $n > 0$, this overestimation is even more pronounced, highlighting the added value of the empirical model (23), which generalizes empirical estimates of FIG wave reflection to rough beds.

4. Discussion

4.1. Comparing the empirical model prediction with laboratory and field observations

The empirical model (23) is obtained based on one-dimensional free propagation of IG waves. Accordingly, this model ignores the presence of sea-swell waves and the effect of the directional distribution on the reflection process. Shoreward of the sea-swell breakpoint, nonlinear coupling of sea-swell and IG waves reduces (e.g., Ruessink, 1998) and a considerable part of the incoming IG energy can be assumed to propagate freely (e.g., Janssen et al., 2003). Nevertheless, detailed analyses of nearshore wave evolution suggest that IG waves in the surfzone can be significantly dissipated as a result of nonlinear transfer of energy from IG waves back to sea-swell (e.g., Thomson et al., 2006; Henderson et al., 2006; Rijnsdorp et al., 2022). Furthermore, sea-swell induced surfzone currents and turbulent motion (e.g., due to wave breaking) may further alter the propagation, dissipation and eventually shoreline reflection of IG waves (e.g., Church and Thornton, 1993).

The directionality of the incoming IG wave field can affect the reflection process in two opposing ways. On the one hand, it can weaken the nonlinear evolution and the associated bore formation and wave breaking, leading to higher reflection values. On the other hand, waves incident obliquely to the shoreline essentially running up over a milder slope than the cross-shore slope, namely, higher directional spreading corresponds to milder effective slope, and thus, to stronger wave dissipation and weaker reflection.

Despite the described limitations of the empirical model, it is desired here to examine its predictive capabilities compared with laboratory and field observations. The considered laboratory observations are obtained from the GLOBEX experiments (Ruessink et al., 2013), which collected cross-shore evolution of short and IG waves over a flume of constant slope ($m = 1/80$). Specifically, the observations of three cases, $A1$, $A2$ and $A3$, describing irregular wave evolution under different incoming wave conditions are examined. In addition, the field observations considered here were collected during September and October 2023 at the Field Research Facility, near Duck, North Carolina

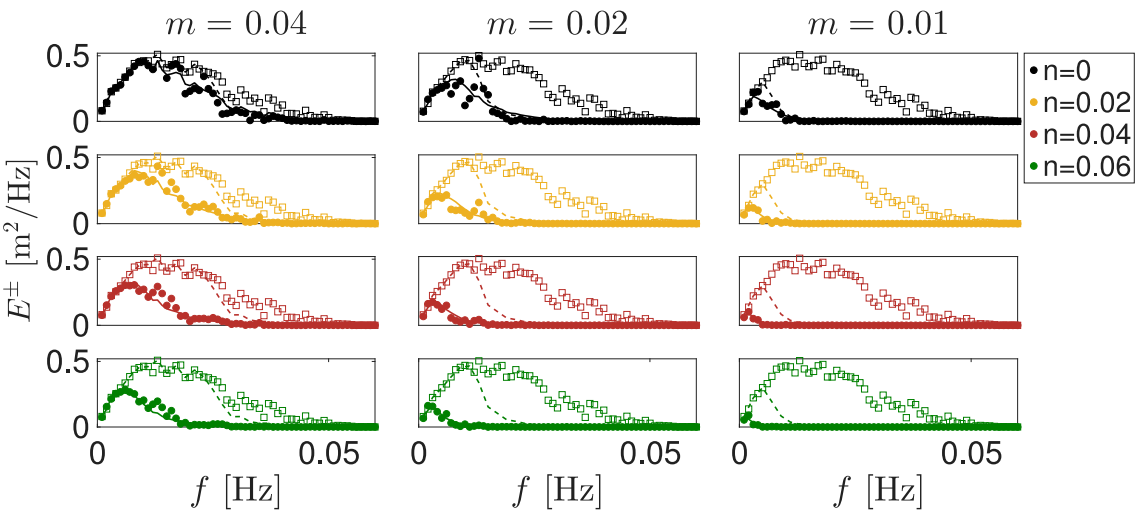


Fig. 10. Incoming (squares) and outgoing FIG spectra for the conditions illustrated in Fig. 2(d). Outgoing predictions are obtained using SWASH (solid circles), the empirical model (23) (solid lines) and the parametrization proposed by Battjes (1974) (16) with β_H defined by (26) (dashed lines).

Table 3
Averaged incoming wave conditions (H_{ig}^{+}, $T_{m,-1,0}$), cross-shore slope (m), water depth (h) and measurement periods of the considered laboratory and field observations.

Name	H_{ig}^{+}	$T_{m,-1,0}$	m	h	Period
GLOBEX A1	0.018 m	17.2 s	1/80	0.078 m	69 min
GLOBEX A2	0.035 m	19.4 s	1/80	0.083 m	69 min
GLOBEX A3	0.024 m	26.0 s	1/80	0.079 m	69 min
Duck23 WC1	0.20 m	73.0 s	1/32	1.383 m	12 h (24/09 00:00–24/09 11:00)
Duck23 WC2	0.16 m	64.7 s	1/29	1.543 m	12 h (24/09 12:00–24/09 23:00)
Duck23 WC3	0.13 m	60.4 s	1/32	1.375 m	12 h (25/09 00:00–25/09 11:00)

(Christensen et al., 2025). More specifically, only the observations collected at Sensor 7, located about 35 m seaward from the shoreline (see upper panel of Fig. 15), are considered. Furthermore, to reduce the uncertainty associated with the cross-shore bathymetry levels, only a one and a half day period around the date of the first bathymetry survey (conducted on September 25) is considered. This one and a half day period is further divided into three 12 h periods which are characterized by different incoming wave conditions and averaged water level. The three field measurement periods are referred to here as 'Duck23 WC1', 'Duck23 WC2' and 'Duck23 WC3'. The wave and bathymetry conditions of the different laboratory and field observations considered here are summarized in Table 3.

Separation of incoming and outgoing waves is performed based on the method of Guza et al. (1984) (using the phase-averaged formulation of Sheremet et al., 2002). The results for the reflection coefficient R are presented in Fig. 11 as a function of ξ_{ig} and are compared with the data collected using SWASH. The results described for GLOBEX were obtained by averaging the results of four collocated wave gauges and current meters in the surfzone, at water depths of about 0.05–0.1 m (based on the 1:20 scaling of GLOBEX, these depths are equivalent to about 1–2 m in the field). On the other hand, the field results represent time average over each of the 12 h time windows considered. Note that, unlike the GLOBEX experiments, the field measurements are subject to a time-varying cross-shore slope. The temporal variation of the slope is taken into account by tracking the water depth at Sensor 7 and based on the bathymetry data detailed in Appendix B.

The bulk reflection results of GLOBEX are consistent with the SWASH dataset and largely follow the $n = 0.01$ sm$^{-1/3}$ curve, with a slight deviation observed for GLOBEX 3. In contrast, the Duck23 reflection results do not follow a single Manning's roughness coefficient, but instead spread between $n = 0.01$ sm$^{-1/3}$ and $n = 0.02$ sm$^{-1/3}$. The average n values inferred from Fig. 11 may partly reflect processes not accounted for in the SWASH dataset due to the presence of sea-swell waves and the directional spreading of the incoming FIG wave field. Nevertheless, these values remain broadly consistent with typical Manning's roughness ranges for the bed types considered, namely $n \in [0.01, 0.02]$ sm$^{-1/3}$ for the concrete flume bed of GLOBEX, and $n \in [0.01, 0.03]$ sm$^{-1/3}$ for the sandy beach of Duck23 (see, e.g., Chow, 1959; Arcement and Schneider, 1989). This consistency suggests that the SWASH dataset and the empirical model (23), derived on its basis, adequately approximate FIG wave reflection at the shoreline.

The agreement between the empirical model (23) and the observation is also evident in the frequency-dependent reflection shown in Fig. 12. The Manning's roughness coefficients used for the predictions are selected based on those inferred from the bulk reflection results in Fig. 11, namely, $n = 0.01$ sm$^{-1/3}$ for GLOBEX and $n = 0.015$ sm$^{-1/3}$ for Duck23. In addition to the comparison with observations, the empirical model is evaluated against predictions from the model of Battjes (1974). The latter consistently overestimates the observed reflection across all six cases considered, whereas predictions using the empirical model closely follow the observed frequency distributions. Note that the agreement of the empirical model with the observations remains reasonable across the range of Manning's roughness values representative of the bed types examined here. This result supports the notion that the one-dimensional reflection of isolated FIG waves, as represented by the SWASH dataset and the derived empirical model, provides an adequate description of the shoreline reflection. However, this suggestion is based on a rather narrow set of observations. Closer investigation into the contributions due to FIG wave directionality and the presence of sea-swell waves under varying bed conditions is needed to draw more robust conclusions.

4.2. The dependence of the reflected energy distribution on the bed properties and wave conditions

The reflection of IG waves along shorelines is commonly considered as the main source of FIG energy offshore. Therefore, adequate description of the shoreline reflection is required for large-scale FIG predictions. Present large-scale predictions of FIG waves describe the seaward radiation of FIG energy through the following frequency distribution:

$$E^{-} = A\,[\min(1, c_1/f)]^{c_2}, \tag{27}$$

where c_1 represents a cut-off frequency beyond which the distribution attenuates as f^{-c_2} and A is a constant. This distribution structure was proposed by Ardhuin et al. (2014) for a global evaluation of shoreline

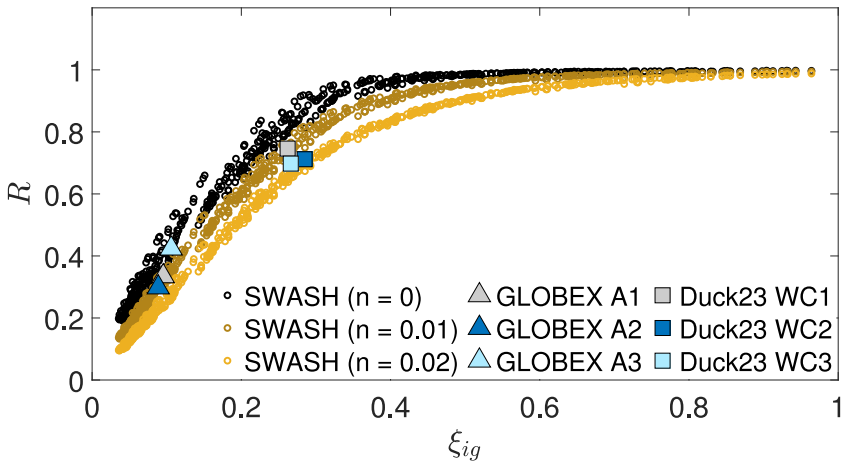


Fig. 11. Laboratory (GLOBEX) and field (Duck23) observations of the bulk reflection coefficient R as a function of ξ_{ig}.

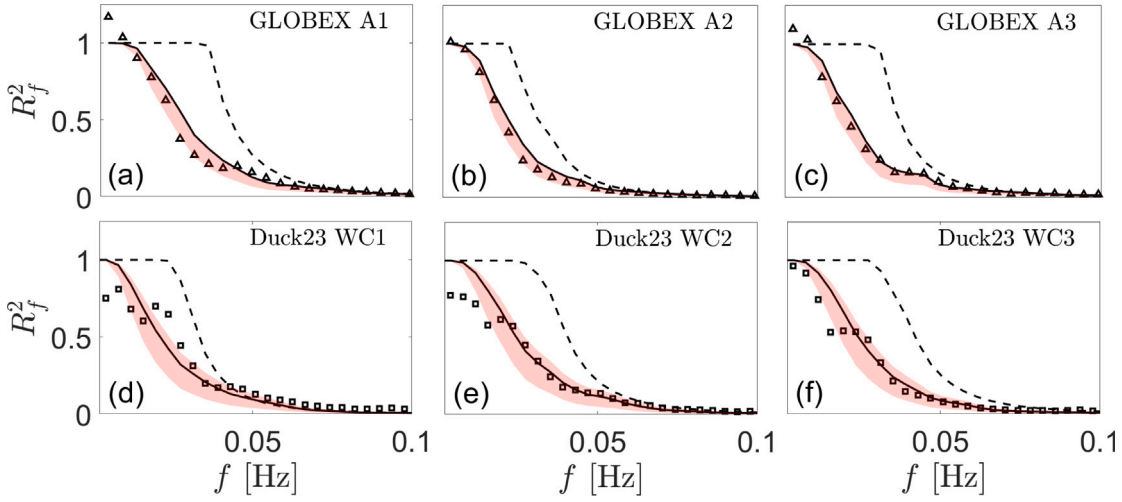


Fig. 12. Frequency-distributed shoreline reflection predicted by the empirical model (solid lines) and the model of Battjes (1974) (dashed lines). Model predictions are compared with observations from (a–c) GLOBEX (triangles) and (d–f) Duck23 (squares). The red shading covers possible model predictions using a Manning's roughness range of (a–c) $n \in [0.01, 0.02]$ sm$^{-1/3}$ and (d–f) $n \in [0.01, 0.03]$ sm$^{-1/3}$.

radiated FIG waves. The parameter values suggested by Ardhuin et al. (2014) to define (27) are $c_1 = 0.015$ Hz and $c_2 = 1.5$. In the following, the suitability of these values are examined under different wave and bathymetry conditions. To this end, E^+ is assumed constant over the IG band such that the empirical model (23) can readily be used to provide a reference for E^- under different bathymetry conditions (represented by m and n) and incoming wave conditions (represented by H_{ig}^+).

Fig. 13 presents the optimal c_1 and c_2 obtained by fitting the distribution structure of (27) to predictions from the empirical model (23). The results indicate that, rather than being universal constants, c_1 and c_2 depend significantly on the wave and bed conditions.

Additionally, Fig. 14 presents four examples illustrating the differences in the predicted E^- when using the optimal c_1 and c_2 values from Fig. 13, compared with the formulation of Ardhuin et al. (2014), while maintaining the same total reflected energy (integrated here over $f = 0.001 - 0.03$ Hz). The results show that, for certain bed conditions, the different distribution formulations can lead to substantial differences in the allocation of energy across lower and higher IG frequencies (as clearly illustrated in the right panels of Fig. 14). These differences at the shoreline boundary can further propagate seaward, leading to different predictions of IG spectral and spatial distributions over large scales. In conclusion, the insights gained here based on the SWASH dataset and the empirical model (23) suggest that reliable prediction of IG waves at large scales requires a shoreline radiation model that accounts for both wave conditions and bed properties.

5. Conclusions

This study presents a numerical investigation of the shoreline dissipation and reflection of FIG waves. To this end, a large dataset was generated with SWASH to characterize the transformation of FIG waves during shoreline reflection across a wide range of wave and bed conditions. It is found that for very mild slopes (i.e., $0.005 \leq m < 0.01$), bottom friction explains most of the shoreline dissipation over rough beds (i.e. $n \geq 0.04$ sm$^{-1/3}$), whereas for sandy beaches (i.e., $n = 0.02$ sm$^{-1/3}$) its contribution typically remains within 25 – 50 %. For steeper slopes (i.e. $m \geq 0.05$), bottom friction becomes the primary dissipation mechanism for both rough and sandy coasts. Under these slope conditions, the ratio of bottom friction and wave breaking dissipation obtains a maximum (which can exceed 2) at a slope that depends on the bed roughness and the incoming wave conditions. These findings deviate from the common assumption that bottom friction plays a secondary role in shoreline dissipation over sandy beaches, and

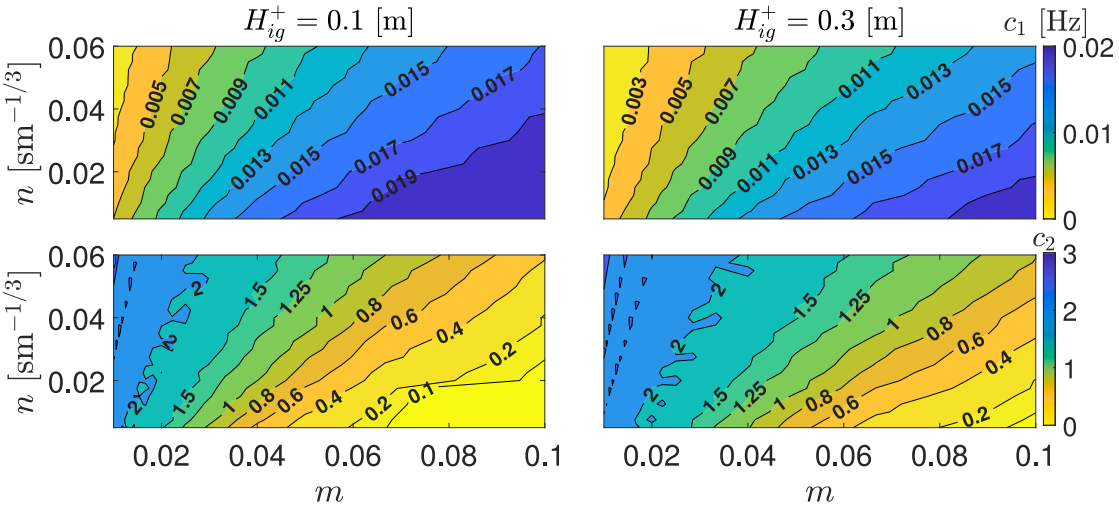


Fig. 13. Optimal cut-off frequency c_1 (upper panels) and attenuation power c_2 (lower panels) obtained by fitting the distribution structure $[\min(1, c_1/f)]^{c_2}$ to the prediction of the empirical model (23), for different m and n and assuming a constant $E^{+}(f)$ corresponding to two different values of H_{ig}^{+}.

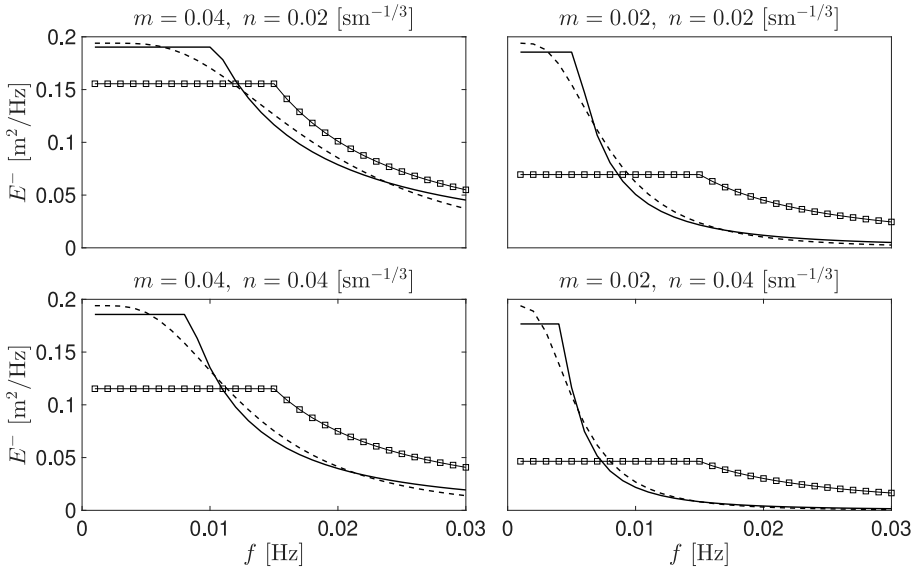


Fig. 14. Predictions of reflected spectra for a constant incoming spectrum characterized by $H_{ig}^{+} = 0.3$ m and for two cross-shore slopes and two Manning's roughness coefficients. Results are obtained using the expression (27) with the optimal c_1 and c_2 values from Fig. 13 (solid lines) and the values proposed by Ardhuin et al. (2014) (lines with squares), where the total reflected energy is kept the same. Predictions from the empirical model (23) are included for reference (dashed lines).

support recent observations highlighting its importance in controlling IG wave reflection over rough shorelines (MacMahan et al., 2026). It should be noted, however, that the findings derived here are based on simulations that neglect directional spreading and the presence of sea-swell waves. Therefore, further studies are required to gain additional insights into the contribution of bottom friction to the dissipation and reflection of IG waves under more realistic wave conditions.

The importance of bottom friction and wave breaking across a wide range of shoreline roughness values highlights the need to account for both processes when evaluating shoreline reflection of FIG waves. Based on the SWASH dataset, an empirical model is derived for frequency-dependent shoreline reflection of FIG waves over both smooth and rough beds. The model performs well even under relatively extreme wave conditions and bed roughnesses (i.e., $H_{ig}^{+} \approx 0.4$ m and $n = 0.06$ sm$^{-1/3}$), and shows good agreement with laboratory and field observations. The latter supports the underlying assumption of the SWASH dataset that, in very shallow water, one-dimensional transformation of isolated FIG waves (i.e., neglecting incoming FIG directionality and the presence of sea-swell waves) can provide a reasonable approximation of the shoreline reflection process. Finally, the empirical model demonstrates that reflection magnitude and spectral distribution depend strongly on incoming wave conditions, cross-shore slope, and bed roughness. Through comparison with the radiation model of Ardhuin et al. (2014), these results further highlight the importance of accounting for these factors when determining radiated FIG energy distributions and associated large-scale IG wave predictions.

In conclusion, the empirical model derived here can be seen as an additional step towards the formulation of an adequate shoreline generation model for large-scale modelling of FIG waves. This contribution complements recent advances in modelling the shoreward transformation of forced IG waves (e.g., Leijnse et al., 2024; Reniers et al., 2026a). Future implementation of these modelling advances within large-scale

modelling frameworks will allow to adequately evaluate the reflection of both locally generated FIG waves and FIG waves originating from remote sources.

CRediT authorship contribution statement

Gal Akrish: Writing – original draft, Methodology, Conceptualization. **Ad Reniers:** Writing – review & editing, Supervision, Conceptualization. **Marcel Zijlema:** Writing – review & editing, Supervision, Software. **Yaron Toledo:** Writing – review & editing, Supervision, Conceptualization.

Declaration of competing interest

The authors declare that they have no known competing financial interests or personal relationships that could have appeared to influence the work reported in this paper.

Acknowledgements

This research was supported by the ISRAEL SCIENCE FOUNDATION (grant 2358/24). The authors would also like to thank Dr. Anouk de Bakker for her insightful suggestions, which helped improve this paper.

Appendix A. A correction factor due to bottom friction

The empirical model (23) is calibrated for bottom friction acting at depths $h \leq 4$ m. Consequently, a correction factor may be required when shoreline reflection is evaluated at depths different from 4 m. Such situations may arise in large-scale modelling applications, where shoreline boundaries extend across regions with varying water depths. To account for this effect, the following mapping is introduced:

$$F^{\pm} = J_0^{\pm} F_0^{\pm} \tag{28}$$

where $F_0^{\pm}$ denotes the incoming or outgoing frequency-dependent flux at the considered depth h_0, $F^{\pm}$ denotes the corresponding flux at $h = 4$ m, and $J_0^{\pm}$ describes transformation due to bottom-friction dissipation between h_0 and h. The correction is applied as follows. First, the incoming flux F_0^{+} is mapped from h_0 and $h = 4$ m using J_0^{+}. The empirical model (23) is then used to determine the outgoing flux F^{-}. Finally, the outgoing flux is mapped back from $h = 4$ m to h_0 using J^{-}. For simplicity, the subscript $\{\}_0$ is omitted in the latter mapping to indicate that J^{-} transforms F^{-} at $h = 4$ m to F_0^{-} at h_0. Combining these steps yields

$$R_{f,0}^2 = J_0^{+} J^{-} R_f^2 \tag{29}$$

where $R_{f,0}^2$ denotes the frequency-dependent reflection at h_0 and R_f^2 is given by (23). This definition, however, violates the expected convergence to one at low frequencies, an artifact that likely results from the implicit assumption made here that the mapping is frequency-independent (see discussion below (35)). A frequency-dependent mapping may resolve this difficulty, but its formulation is presently unknown. Therefore, the following alternative expression is proposed:

$$R_{f,0}^2 = \tanh^{p}\left[J_0^{+} J^{-} \frac{n_0 m}{n_0 + n} \left(\frac{g^{1.5}}{c\sqrt{F^{+}} f^3} \right)^{1/r} \right] \tag{30}$$

which preserves the limits at low and high frequencies and numerically shows relatively small global (in terms of f) error comparing to (29). The predictive capability of the empirical model with the friction correction (30) is demonstrated in Fig. 9. Finally, the formulation of (30) is completed through the derivation of the mapping function J.

The mapping function J is derived under the following assumptions. First it is assumed that both h_0 and h are located over a constant sloping bed m within the shoaling zone (i.e., seaward of the breakpoint depth). The derivation further assumes quasi-linear wave transformation over shallow waters. Finally, it should be noted that the following derivation closely follows Thornton and Guza (1983).

Under these assumptions, the derivation starts from (6), neglecting the wave breaking dissipation term. Under the assumption of narrow-banded linear wave field and following the bottom friction formulation (8), the phase-averaged expression of D_f for a single wave can be written as

$$D_f = c_f \left(\frac{g}{h} \right)^{3/2} \frac{H^3}{6\pi} \tag{31}$$

Under the quasi-linear assumption, H is assumed to follow a Rayleigh distribution, yielding the following ensemble-averaged dissipation for a random wave field:

$$D_f = c_f \left(\frac{g}{h} \right)^{3/2} \frac{H_{rms}^3}{8\sqrt{\pi}} \tag{32}$$

where (32) differs from the corresponding expression of Thornton and Guza (1983) (their Eq. 40) by a factor of two, as discussed in Appendix B of Marques et al. (2025). Finally, by substituting $H_{rms} = \sqrt{8\bar{F}/\sqrt{gh}}$ and using (32), the starting-point Eq. (6) reduces to

$$\frac{d\bar{F}^{\pm}}{dh} = \pm C_d \frac{\bar{F}^{\pm 3/2}}{h^{9/4}}. \tag{33}$$

where the derivative with respect to x is transformed into a derivative with respect to h through the relation $h = h_0 - mx$, C_d is defined as

$$C_d = \sqrt{\frac{8}{\pi}} \frac{c_f}{m\, g^{1/4}} \tag{34}$$

and c_f is the friction coefficient which can be defined as a constant or as a depth-dependent term. Eq. (33) can be solved analytically (following an approach similar to that used by Thornton and Guza, 1983 for the wave breaking model presented in Eq. 27 of their study), yielding

$$\bar{F}^{\pm} = J_0^{\pm} \bar{F}_0^{\pm}$$
$$J_0^{\pm} = \frac{1}{\left[1 \pm \frac{C_d \sqrt{\bar{F}_0^{\pm}}}{2(q-1)h_0^{q-1}} \left(\left(\frac{h_0}{h} \right)^{q-1} - 1 \right) \right]^2} \tag{35}$$

where q depends on the definition of c_f. For constant c_f, $q = 9/4$, whereas using Manning's formulation, for which $c_f \propto h^{-1/3}$, $q = 31/12$. It should be emphasized that $J_0^{\pm}$ is derived for the bulk fluxes $\bar{F}_0^{\pm}$ and $\bar{F}^{\pm}$. Applying (28) to the frequency-dependent fluxes therefore assumes that the bulk dissipation is distributed in proportion with $F_0^{\pm}$. This assumption is analogous to the proportional distribution commonly adopted for wave breaking dissipation in spectral wave models (Eldeberky and Battjes, 1996).

Appendix B. Bathymetric data used for the analysis of the field observations

The cross-shore bathymetry along the transect crossing Sensor 7 is presented in Fig. 1 of Christensen et al. (2025). For convenience, the same bathymetric profile is reproduced here in the upper panel of Fig. 15.

The hourly-averaged shoreline reflection evaluated based on the empirical model (23) requires the hourly-averaged values of m. These values are shown in the lower panels of Fig. 15 for each of the examined measurements periods. The presented hourly-averaged m are defined as the cross-shore slope around $x(h = 0)$. The latter is determined based on the hourly-averaged water depth measured at Sensor 7 and corresponds to the cross-shore position where the bed elevation intersects the hourly-averaged water level. An example of the resulting $x(h = 0)$ location is indicated by the cross in the upper panel of Fig. 15.

Data availability

Data will be made available on request.

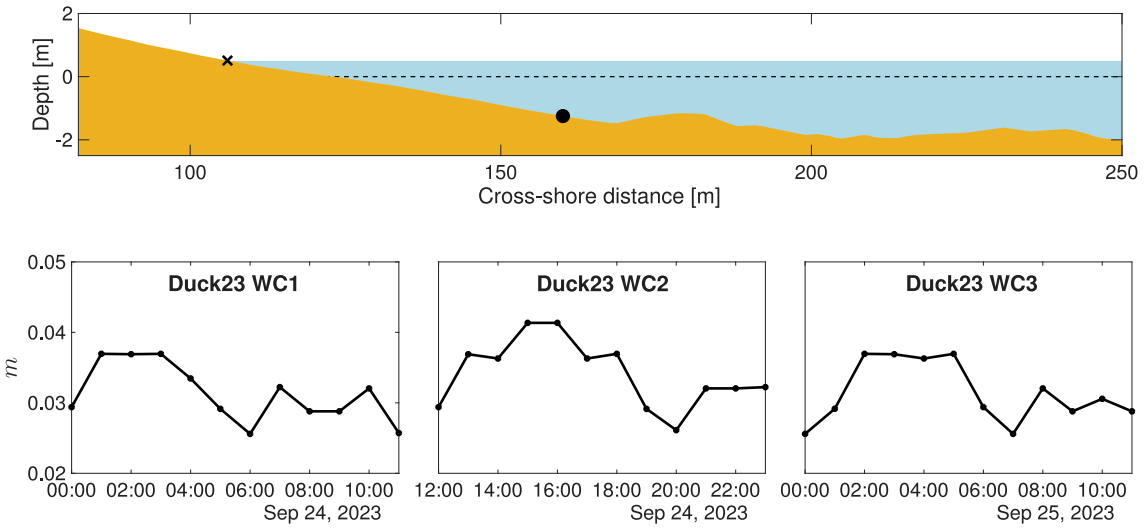


Fig. 15. Upper panel: Cross-shore bathymetric profile along the Sensor 7 transect. The yellow fill indicates the bed profile, the dashed horizontal line denotes mean sea level, the black dot marks the location of Sensor 7, and the cross indicates the location $x(h = 0)$ used for the estimation of the cross-shore slope m. Lower panels: Hourly-averaged cross-shore slopes used for the prediction of shoreline reflection.

References

Ahn, S., 2021. Modeling mean relation between peak period and energy period of ocean surface wave systems. Ocean Eng. 228, 108937.

Akrish, G., Reniers, A., Rijnsdorp, D., Zijlema, M., Rutten, J., Tissier, M., 2025. The importance of free infragravity waves in the North Sea: Insights from field observations and unstructured SWAN modelling. Ocean. Model. 102619.

Akrish, G., Reniers, A., Zijlema, M., Smit, P., 2024. QuadWave1D: An optimized quadratic formulation for spectral prediction of coastal waves. Coast. Eng. 191, 104516.

Arcement, G., Schneider, V., 1989. Guide for Selecting Manning's Roughness Coefficients for Natural Channels and Flood Plains. US Government Printing Office.

Ardhuin, F., Rawat, A., Aucan, J., 2014. A numerical model for free infragravity waves: Definition and validation at regional and global scales. Ocean. Model. 77, 20–32.

Ardhuin, F., Roland, A., 2012. Coastal wave reflection, directional spread, and seismoacoustic noise sources. J. Geophys. Res.: Ocean. 117 (C11).

Battjes, J.A., 1974. Surf similarity. Coast. Eng. Proc. (14), 466–480.

Baumann, J., Chaumillon, E., Bertin, X., Schneider, J.-L., Guillot, B., Schmutz, M., 2017. Importance of infragravity waves for the generation of washover deposits. Mar. Geol. 391, 20–35.

Bertin, X., de Bakker, A., van Dongeren, A., Coco, G., André, G., Ardhuin, F., Bonneton, P., Bouchette, F., Castelle, B., Crawford, W.C., Davidson, M., Deen, M., Dodet, G., Guérin, T., Inch, K., Leckler, F., McCall, R., Muller, H., Olabarrieta, M., Roelvink, D., Ruessink, G., Sous, D., Stutzmann, É., Tissier, M., 2018. Infragravity waves: From driving mechanisms to impacts. Earth-Sci. Rev. 177, 774–799.

Booij, N., Ris, R.C., Holthuijsen, L.H., 1999. A third-generation wave model for coastal regions: 1. Model description and validation. J. Geophys. Res.: Ocean. 104 (C4), 7649–7666.

Bowers, E., 1977. Harbour resonance due to set-down beneath wave groups. J. Fluid Mech. 79 (1), 71–92.

Bromirski, P.D., Sergienko, O.V., MacAyeal, D.R., 2010. Transoceanic infragravity waves impacting Antarctic ice shelves. Geophys. Res. Lett. 37 (2).

Bunya, S., Dietrich, J.C., Westerink, J., Ebersole, B., Smith, J., Atkinson, J., Jensen, R., Resio, D., Luettich, R., Dawson, C., et al., 2010. A high-resolution coupled riverine flow, tide, wind, wind wave, and storm surge model for southern Louisiana and Mississippi. Part I: Model development and validation. Mon. Weather Rev. 138 (2), 345–377.

Chow, V.T., 1959. Open-Channel Hydraulics. McGraw–Hill, New York.

Christensen, D.F., Raubenheimer, B., Elgar, S., 2025. Observations of sea-swell wave reflection from a steep, nearshore bar. Earth Space Sci. 12 (4), e2024EA004176.

Church, J.C., Thornton, E.B., 1993. Effects of breaking wave induced turbulence within a longshore current model. Coast. Eng. 20 (1–2), 1–28.

De Bakker, A., Tissier, M., Ruessink, B., 2014. Shoreline dissipation of infragravity waves. Cont. Shelf Res. 72, 73–82.

De Bakker, A., Tissier, M., Ruessink, B., 2016. Beach steepness effects on nonlinear infragravity-wave interactions: A numerical study. J. Geophys. Res.: Ocean. 121 (1), 554–570.

Dekkers, J., 2018. Undular Bore Development Over Coral Reefs an Experimental Study (MSc Thesis). Delft University of Technology.

Dingemans, M.W., 1997. Water Wave Propagation over Uneven Bottoms. In: Advanced Series on Ocean Engineering, Vol. 13, World Scientific.

Dodet, G., Melet, A., Ardhuin, F., Bertin, X., Idier, D., Almar, R., 2019. The contribution of wind-generated waves to coastal sea-level changes. Surv. Geophys. 40 (6), 1563–1601.

Eldeberky, Y., Battjes, J.A., 1996. Spectral modeling of wave breaking: Application to Boussinesq equations. J. Geophys. Res.: Ocean. 101 (C1), 1253–1264.

Elgar, S., Herbers, T., Guza, R., 1994. Reflection of ocean surface gravity waves from a natural beach. J. Phys. Oceanogr. 24 (7), 1503–1511.

Elgar, S., Herbers, T., Okihiro, M., Oltman-Shay, J., Guza, R., 1992. Observations of infragravity waves. J. Geophys. Res.: Ocean. 97 (C10), 15573–15577.

Guza, R., Thornton, E., Holman, R., 1984. Swash on steep and shallow beaches. Coast. Eng. Proc. (19), 48.

Hasselmann, K., 1962. On the non-linear energy transfer in a gravity-wave spectrum Part 1. General theory. J. Fluid Mech. 12 (4), 481–500.

Henderson, S.M., Guza, R., Elgar, S., Herbers, T., Bowen, A., 2006. Nonlinear generation and loss of infragravity wave energy. J. Geophys. Res.: Ocean. 111 (C12).

Herbers, T., Elgar, S., Guza, R., O'reilly, W., 1995. Infragravity-frequency (0.005–0.05 Hz) motions on the shelf. Part II: Free waves. J. Phys. Oceanogr. 25 (6), 1063–1079.

Holthuijsen, L.H., 2010. Waves in Oceanic and Coastal Waters. Cambridge University Press.

Huntley, D., Guza, R., Bowen, A., 1977. A universal form for shoreline run-up spectra? J. Geophys. Res. 82 (18), 2577–2581.

Janssen, T., Battjes, J., Van Dongeren, A., 2003. Long waves induced by short-wave groups over a sloping bottom. J. Geophys. Res.: Ocean. 108 (C8).

Lashley, C.H., Jonkman, S.N., Van der Meer, J., Bricker, J.D., Vuik, V., 2022. The influence of infragravity waves on the safety of coastal defences: A case study of the Dutch Wadden Sea. Nat. Hazards Earth Syst. Sci. 22 (1), 1–22.

Leijnse, T.W., van Ormondt, M., van Dongeren, A., Aerts, J.C., Muis, S., 2024. Estimating nearshore infragravity wave conditions at large spatial scales. Front. Mar. Sci. 11, 1355095.

Mackie, L., Evans, P.S., Harrold, M.J., ODoherty, T., Piggott, M.D., Angeloudis, A., 2021. Modelling an energetic tidal strait: Investigating implications of common numerical configuration choices. Appl. Ocean Res. 108, 102494.

MacMahan, J., Feddersen, F., Reniers, A., Thornton, E., Marques, O., 2026. Infragravity Waves Across a Steeper-Sloping Rough Rocky Seabed on the Inner Shelf. J. Geophys. Res.: Ocean. 131 (9), e2025JC023188.

Marques, O.B., Feddersen, F., MacMahan, J., Acevedo-Ramirez, C.A., Suanda, S.H., 2025. Observations of wave energy dissipation by bottom friction on rocky shores. J. Phys. Oceanogr. 55 (5), 593–610.

Matsuba, Y., Roelvink, D., van Dongeren, A., 2024. Propagation of free infragravity waves generated at distant beaches. J. Geophys. Res.: Ocean. 129 (10), e2023JC020580.

McCall, R.T., De Vries, J.V.T., Plant, N., Van Dongeren, A., Roelvink, J., Thompson, D., Reniers, A., 2010. Two-dimensional time dependent hurricane overwash and erosion modeling at Santa Rosa Island. Coast. Eng. 57 (7), 668–683.

Miche, R., 1951. Le pouvoir réfléchissant des ouvrages maritimes exposés à l'action de la houle. Ann. Ponts Chaussees 121, 285–319.

Okihiro, M., Guza, R., Seymour, R., 1992. Bound infragravity waves. J. Geophys. Res.: Ocean. 97 (C7), 11453–11469.

Okihiro, M., Guza, R., Seymour, R., 1993. Excitation of seiche observed in a small harbor. J. Geophys. Res.: Ocean. 98 (C10), 18201–18211.
Peregrine, D.H., 1966. Calculations of the development of an undular bore. J. Fluid Mech. 25 (2), 321–330.
Rawat, A., Ardhuin, F., Ballu, V., Crawford, W., Corela, C., Aucan, J., 2014. Infragravity waves across the oceans. Geophys. Res. Lett. 41 (22), 7957–7963.
Reniers, A., Akrish, G., Zijlema, M., 2026a. A local phase-shift approach for predicting wave-group-forced infragravity waves under directional seas. Coast. Eng. 104946.
Reniers, A.J., Naporowski, R., Tissier, M.F., de Schipper, M.A., Akrish, G., Rijnsdorp, D.P., 2021. North sea infragravity wave observations. J. Mar. Sci. Eng. 9 (2), 141.
Reniers, A., Zijlema, M., 2022. SWAN surfbeat-1D. Coast. Eng. 172, 104068.
Reniers, A., et al., 2026b. SWAN modeling of infragravity waves during REFLEX. Manuscript in preparation.
Rijnsdorp, D.P., Reniers, A.J., Zijlema, M., 2021. Free infragravity waves in the North Sea. J. Geophys. Res.: Ocean. 126 (8), e2021JC017368.
Rijnsdorp, D.P., Smit, P.B., Guza, R., 2022. A nonlinear, non-dispersive energy balance for surfzone waves: infragravity wave dynamics on a sloping beach. J. Fluid Mech. 944, A45.
Rijnsdorp, D.P., Smit, P.B., Zijlema, M., 2014. Non-hydrostatic modelling of infragravity waves under laboratory conditions. Coast. Eng. 85, 30–42.
Roeber, V., Bricker, J.D., 2015. Destructive tsunami-like wave generated by surf beat over a coral reef during Typhoon Haiyan. Nat. Commun. 6 (1), 7854.
Roelvink, D., Reniers, A., Van Dongeren, A., De Vries, J.V.T., McCall, R., Lescinski, J., 2009. Modelling storm impacts on beaches, dunes and barrier islands. Coast. Eng. 56 (11–12), 1133–1152.
Ruessink, B., 1998. Bound and free infragravity waves in the nearshore zone under breaking and nonbreaking conditions. J. Geophys. Res.: Ocean. 103 (C6), 12795–12805.
Ruessink, B.G., Michallet, H., Bonneton, P., Mouazé, D., Lara, J., Silva, P.A., Wellens, P., 2013. Globex: wave dynamics on a gently sloping laboratory beach. Proc. Coast. Dyn. 1351–1362.
Ruggiero, P., Holman, R.A., Beach, R., 2004. Wave run-up on a high-energy dissipative beach. J. Geophys. Res.: Ocean. 109 (C6).
Sheremet, A., Guza, R., Elgar, S., Herbers, T., 2002. Observations of nearshore infragravity waves: Seaward and shoreward propagating components. J. Geophys. Res.: Ocean. 107 (C8), 10–11.
Smit, P., Zijlema, M., Stelling, G., 2013. Depth-induced wave breaking in a non-hydrostatic, near-shore wave model. Coast. Eng. 76, 1–16.
Thomson, J., Elgar, S., Raubenheimer, B., Herbers, T., Guza, R., 2006. Tidal modulation of infragravity waves via nonlinear energy losses in the surfzone. Geophys. Res. Lett. 33 (5).
Thornton, E.B., Guza, R., 1983. Transformation of wave height distribution. J. Geophys. Res.: Ocean. 88 (C10), 5925–5938.
Tolman, H.L., 1991. A third-generation model for wind waves on slowly varying, unsteady, and inhomogeneous depths and currents. J. Phys. Oceanogr. 21 (6), 782–797.
Turner, I.L., Leaman, C.K., Harley, M.D., Thran, M.C., David, D.R., Splinter, K.D., Matheen, N., Hansen, J.E., Cuttler, M.V., Greenslade, D.J., Zieger, S., Lowe, R.J., 2024. A framework for national-scale coastal storm hazards early warning. Coast. Eng. 192, 104571.
Van Dongeren, A., Battjes, J., Janssen, T., Van Noorloos, J., Steenhauer, K., Steenbergen, G., Reniers, A., 2007. Shoaling and shoreline dissipation of low-frequency waves. J. Geophys. Res.: Ocean. 112 (C2).
Vrecica, T., Toledo, Y., 2019. Consistent nonlinear deterministic and stochastic wave evolution equations from deep water to the breaking region. J. Fluid Mech. 877, 373–404.
Webb, S.C., Zhang, X., Crawford, W., 1991. Infragravity waves in the deep ocean. J. Geophys. Res.: Ocean. 96 (C2), 2723–2736.
Winter, G., Storlazzi, C., Vitousek, S., Van Dongeren, A., McCall, R., Hoeke, R., Skirving, W., Marra, J., Reyns, J., Aucan, J., et al., 2020. Steps to develop early warning systems and future scenarios of storm wave-driven flooding along coral reef-lined coasts. Front. Mar. Sci. 7, 199.
Zanuttigh, B., Van der Meer, J.W., 2006. Wave reflection from coastal structures. Coast. Eng. Proc. (30), 4337–4349.
Zijlema, M., Stelling, G., Smit, P., 2011. SWASH: An operational public domain code for simulating wave fields and rapidly varied flows in coastal waters. Coast. Eng. 58 (10), 992–1012.